Applied Catalysis B: Environmental 304 (2022) 120925

Contents lists available at ScienceDirect

Applied Catalysis B: Environmental

journal homepage: www.elsevier.com/locate/apcatb

Co@C nanorods as both magnetic stirring nanobars and magnetic recyclable nanocatalysts for microcatalytic reactions

Tianyu Zhang, Huijing Wang, Xiaodi Guo, Shiheng Shao, Lei Ding, Aijuan Han, Lianying Wang *, Junfeng Liu *

State Key Laboratory of Chemical Resource Engineering, Beijing University of Chemical Technology, Beijing 100029, PR China

ARTICLE INFO

Keywords:
Nanorod
Carbon embedded nanoparticles
Heterogeneous catalyst
Nanoscale magnetic stirring bar

ABSTRACT

The rapid and effective mixing of reactants and catalysts is essential in liquid-phase catalytic reaction to boost mass transport. However, the routinely used magnetic stirring method is impractical for ultra-small systems such as lab-on-chip and flow cell due to the macroscale size of the magnetic bars. Herein, we developed a facile strategy to synthesize catalytically active magnetic Co@C nanorods, which could serve as both high-performance catalysts and magnetic stirring nanobars for micro-catalytic reactions. The Co@C core-shell structure endows the materials with high catalytic activity and excellent durability, while the strong magnetism of Co nanoparticles renders the nanorod catalyst unique stirring capability under an external rotating magnetic field, which significantly promotes the mass transport and also the catalytic efficiency in micro-catalytic reactions. Inspired by the unique structure and properties, the mixing ability and catalytic activity of Co@C nanorods were evaluated in several systems.

1. Introduction

Diffusion, as the primary mechanism of mass transport, is one of the key factors in determining the catalytic efficiency in heterogeneous catalysis [1]. Commercial magnetic stirring bars are typically used to remit the passive diffusion sluggish in the liquid-phase catalytic reaction. However, such a macroscale strategy is impractical for ultra-small systems, e.g. microfluidics, microdroplets, or flow cells, which play important parts in lab-on-chip applications and microliter bioassay [2,3]. Besides, trace amounts of active components trapped on the surface of reused magnetic stirring bars may mislead the performance evaluation of the catalysts [4]. Several mixing strategies were developed without employing magnetic stirring bars, by using pressure, temperature gradient, ultrasound waves, or electric field, which however require ingeniously designed devices and make the strategies costly and inflexible [5,6]. Recently, one-dimensional (1D) magnetic nanorods with unique anisotropic properties and rigid bar structure show great potential as nano-stirring bars in micro-reactors [7–9], which can be applied in the practical microcatalytic process without the additional complicated mixing technique. The external magnetic field can guide the assembly of magnetic nanorods building into periodically aligned arrays dispersed uniformly in the solution, which is beneficial to the formation of micro-vortex and thus boost the mass transport [10,11]. Impressively, magnetic nanocatalysts, combining both the high activity of catalytic sites and strong magnetism of magnetic nanoparticles, attract much attention due to the stirring capability in an external rotating magnetic field [12] and the recyclability without the loss of the catalytic efficiency [13]. However, most of the reported 1D magnetic catalysts consist of iron-based nanoparticles (NPs) as magnetic substance, silicon dioxide or polymer as 1D protective coating materials and additional noble metal species as catalytic active centers, which makes the synthesis procedure costly with multiple steps and the uniformity of the products is affected greatly by imperceptible factors [14,15]. The protective coating materials avoid the loss of magnetic species, however, they always reduce saturation magnetization of the obtained magnetic catalysts, exhibiting a poor magnetic responsivity towards the external magnetic field [16]. Hence, the preparation of magnetic stirring nanobars with high saturation magnetization through a facile strategy remains a considerable challenge.

As another key aspect of catalysis, the rational design of size-controlled catalysts with both high activity and stability is of great importance [17]. Transition metal NPs with uniform dispersion and narrow nano-size distribution embedded in 1D graphitic carbon nanorod (M@C) have recently received sufficient attention, which show

* Corresponding authors.
E-mail addresses: wangliany@mail.buct.edu.cn (L. Wang), ljf@mail.buct.edu.cn (J. Liu).

https://doi.org/10.1016/j.apcatb.2021.120925
Received 30 August 2021; Received in revised form 23 October 2021; Accepted 9 November 2021
Available online 16 November 2021

several significant superiorities [18,19]: (1) the use of 1D carbon nanorod as support allows the uniform dispersion and high atomic utilization of active metal components; (2) the synergistic effect between the graphite carbon shell and the metal NPs core promotes higher efficiency and selectivity in the catalytic process; (3) the carbon shell can sufficiently prevent the metal core deactivation by isolating the catalytic active centers from the harsh reaction environment; (4) more importantly, when catalytic active metal NPs with the magnetic property was embedded, the obtained M@C core/shell nanocatalysts can act as both stirring bar and catalyst, which will benefit the mass transport [20,21]. Several methods have been proposed to fabricate size-controlled M@C nanorod including electrospun, solution-phase route, and electrochemical deposition [22,23], however, current methods either require poisonous, corrosive organic reagents, expensive, tedious processes or not applicable to mass production, which hinders their practical application [24]. The fabrication of M@C nanorods with uniform dispersion and narrow nano-size distribution through a facile, inexpensive, and large-scale route is still challenged [25].

Herein, we present the cost-effective synthesis of uniformly dispersed Co NPs embedded in graphitic carbon nanorods through direct pyrolysis of salicylate anions intercalated cobalt hydroxide nanorods as both precursor and template. The strong coordination between organic salicylate anions and inorganic cobalt ions reduces the agglomeration of Co species during pyrolysis, facilitating the formation of Co NPs with uniform dispersion and narrow nano-size distribution. Besides, the graphite carbon shell transformed from organic linkers averts the damage of embedded metal NPs, which guaranteed outstanding stability. The size of Co NPs can be easily tuned by changing the pyrolysis temperature to adjust the catalytic activity and magnetic property of the catalysts. As a result, the as-prepared Co@C catalyst at a pyrolysis temperature of 750 °C exhibits outstanding magnetic response (with a high saturation magnetization up to 153.8 emu g^{-1}) and promising mixing ability under an external rotating magnetic field, which can be considered as ideal nanoscale magnetic stirring bars. Moreover, as a stirring nanocatalysts, Co@C nanorods show excellent catalytic activity and can be easily recycled and reused without the loss of the catalysts in both macro and micro systems, demonstrated by the catalytic reduction of 4-nitrophenol (4-NP) or methylene blue (MB) as probe reactions.

2. Experimental

2.1. Synthesis of $Co(OH)(C_6H_5CO_3)\cdot H_2O$ precursor.

The precursor was prepared by a simple coprecipitation method. In a typical procedure, the $Co(NO_3)_2.6H_2O$ (0.04 mol) and $C_7H_5O_3Na$ (0.08 mol) were mixed in the 500 mL deionized water in a four-necked flask. To control the pH at 7.0, 1 M NaOH solution was added into the flask drop by drop through the dropping funnel and the mixture was stirred at 90 °C for 24 h. Thereafter, the precipitates were separated by centrifugation, washed repeatedly, and dried in a vacuum oven overnight at 50 °C.

2.2. Synthesis of Co@C nanofiber

The as-obtained $Co(OH)(C_6H_5CO_3)\cdot H_2O$ precursor loaded in a ceramic boat were placed at the center of a tube-furnace under continuous flow (40 mL cm^{-2} min^{-1}) of N_2 gas. The furnace temperature was raised at a ramping rate of 5 °C min^{-1} and then kept at a specified temperature for 2 h.

2.3. Characterizations

X-ray diffraction (XRD) patterns were recorded on a Shimadzu XRD-6000 diffractometer operated at 40 kV and 30 mA with Cu Kα radiation (λ = 0.15406 nm). The morphology of samples was obtained with Hitachi S-4700 field emission scanning electron microscopy (SEM) at 20 kV. The corresponding Energy-dispersive X-ray spectroscopy (EDX) was used for qualitative elemental chemical analysis. Transmission electron microscopy (TEM) and high-resolution transmission electron microscopy (HRTEM) have also been used for morphological studies with Hitachi HT-7700 at 100 kV and JEOL JEM-2010 at 200 kV, respectively. Raman spectroscopy was performed on a Renishaw RM2000 confocal Raman spectrometer with a 514 nm excitation laser. Fourier transform infrared spectra (FT-IR) were recorded in the range 4000–400 cm^{-1} with 2 cm^{-1} resolution on a Bruker Vector-22 Fourier transform spectrometer using the KBr pellet technique (1 mg of sample in 100 mg of KBr). X-ray photoelectron spectra (XPS) were recorded on a Thermo VG ESCALAB 250 X-ray photoelectron spectrometer at a pressure of about 2×10^{-9} Pa using Al Kα X-rays as the excitation source. The specific surface area and pore volume and size analysis were performed by the Brunauer-Emmett-Teller (BET) and Barrett-Joyner-Halenda (BJH) methods respectively using a Quantachrome Autosorb-1C-VP Analyzer. Prior to the measurements, samples were degassed at 100 °C for 10 h. The magnetic properties of the microspheres were measured on a Lake Shore 7410 vibrating sample magnetometer (VSM) at room temperature. The electron paramagnetic resonance (EPR) spectra were collected on an EMX-500 spectrometer with a center field at 3320 G and a sweep width of 140 G at room temperature. The concentrations of cobalt were determined using inductively coupled plasma atomic emission spectroscopy (ICP-AES). The liquid chromatography-mass spectrometry (LC-MS) was collected on QTRAP5500 with a *m/z* range of 5–1000 amu.

2.4. Macro-catalytic reaction measurements

The reduction reaction of 4-nitrophenol by $NaBH_4$ was used as a model system to quantitatively evaluate the catalytic activity of the as-synthesized nanocomposites. In a typical procedure, the aqueous solutions of 4-nitrophenol (5 mM) and $NaBH_4$ (1.5 M) were freshly prepared. 2 mL of $NaBH_4$ solution and a certain amount of catalysts were added to 100 mL of DI water. Then, 2 mL of 4-nitrophenol solution was injected into the mixture to start the reaction. During the reaction process, 1 mL of the reaction solution was extracted from the reaction system at a regular time, and diluted with 2 mL of DI water followed by measuring UV–vis spectra of the solution to monitor the concentration of 4 -nitrophenol through its absorption peak at 400 nm.

2.5. Flow cell reaction measurements

5 mg catalyst dispersion was inlet into the home-made flow cell with S channel (25 cm in total length and 3 mm in diameter) and immobilized by the magnetic field. The flow cell was placed on a turn-on/off magnetic stirrer with a rotate speed of 300 rpm. Afterwards, the mixture of MB (1.25×10^{-5} mol L^{-1}) and PMS (2.7×10^{-4} mol L^{-1}) solution was continuous through. The flow rate was 5 mL min^{-1}. The outlet solution was immediately quenched with 0.3 mL of sodium sulfite solution (0.1 mol L^{-1}) and measured by UV–vis spectra.

2.6. Micro-catalytic reaction measurements

Onto a glass pane placed on a turn-on/off magnetic stirrer with a rotate speed of 300 rpm, 40 μL of MB (1.25×10^{-5} mol L^{-1}) and PMS (2.7×10^{-4} mol L^{-1}) solution was dropped. Then 7 μL of the Co@C, Co@C-650 and Co@C-850 dispersion solution (3 mg mL^{-1}) or $CoCl_2.6H_2O$ (6 mg mL^{-1}) was injected into the droplets. The tiny Co@C nanocatalysts were churning in the droplet, and the blue color faded subsequently, whereas the droplet without any catalyst stayed blue all the time.

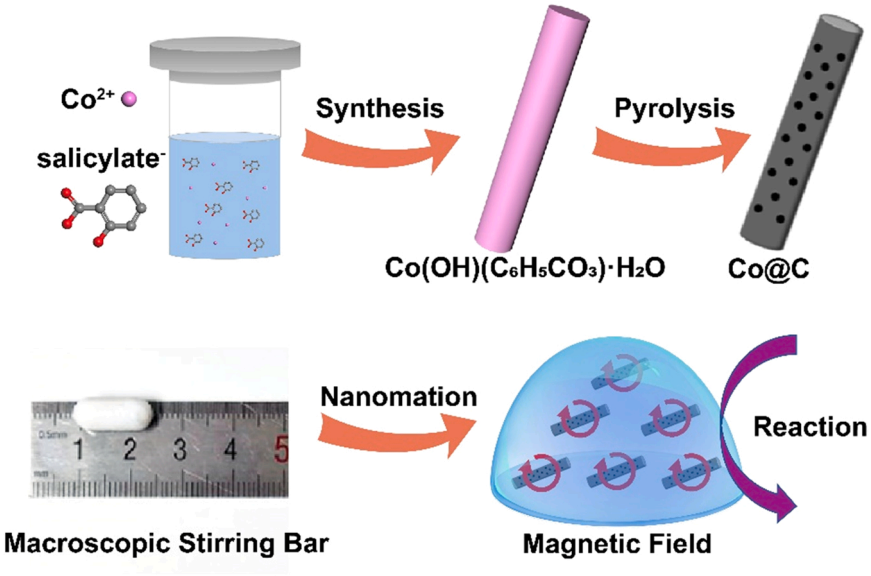

Scheme 1. Schematic illustration of the preparation procedure of Co@C as both nanoscale magnetic stirring bar and catalyst for highly efficient catalysis with fast diffusion.

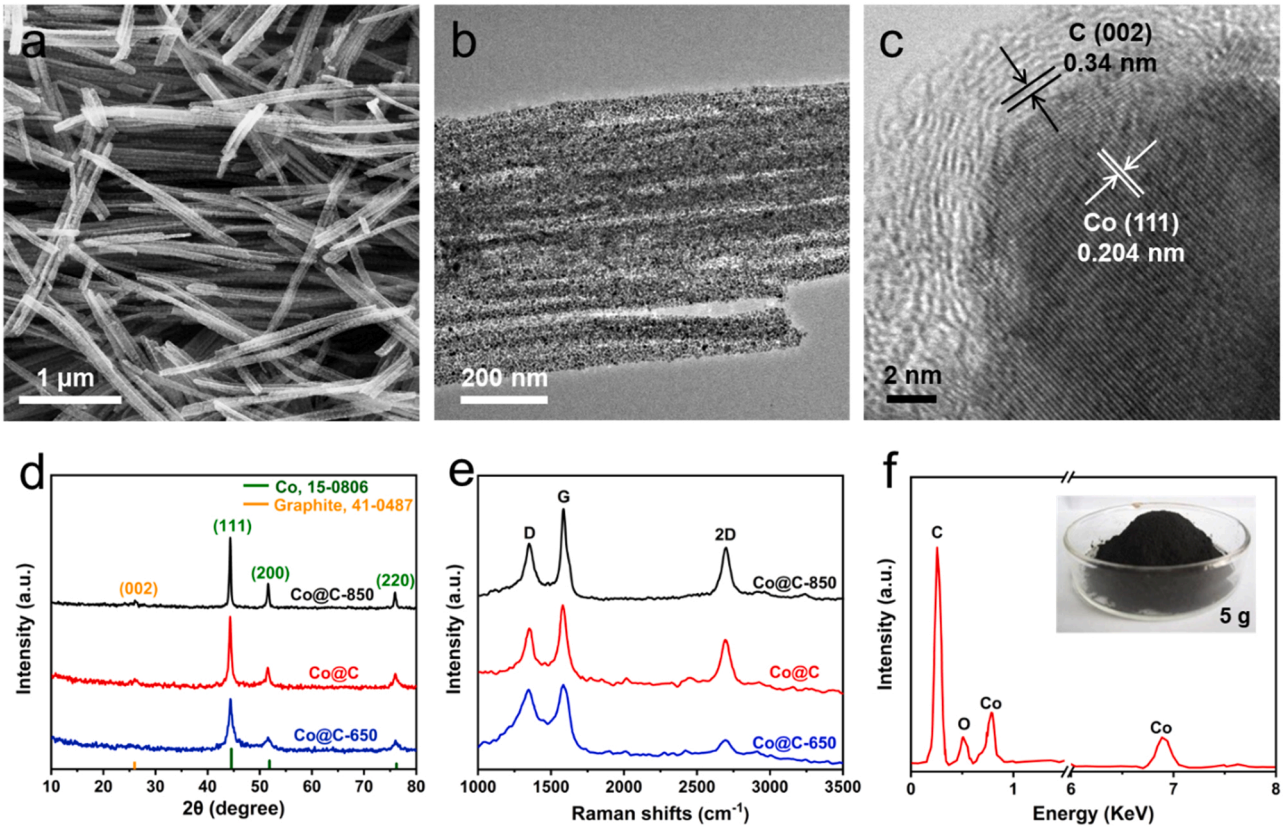

Fig. 1. (a) SEM, (b) TEM and (c) HRTEM images of Co@C. (d) XRD patterns and (e) Raman spectra (f) of Co@C with different pyrolysis temperatures. (f) EDX spectrum of Co@C (the inset photo showing the production of Co@C in the gram scale).

3. Results and discussion

3.1. Large scale synthesis and structural characterization of 1D Co@C nanorods

Scheme 1 illustrates the synthetic procedure of the Co@C nanorods derived from salicylate anions intercalated cobalt hydroxide (Co(OH)($C_6H_5CO_3$)·H_2O) nanorods, which can work as both catalysts and nanoscale magnetic stirring bars for highly efficient catalysis with fast diffusion. The precursor Co(OH)($C_6H_5CO_3$)·H_2O with a typical layered structure of layered hydroxide salts (Fig. S1) was first prepared [26]. Scanning electron microscopy (SEM) image reveals that the precursors were parallel-aligned nanorods with ~100 nm in diameter and several micrometers in length (Fig. S2). When annealing Co(OH)($C_6H_5CO_3$)·

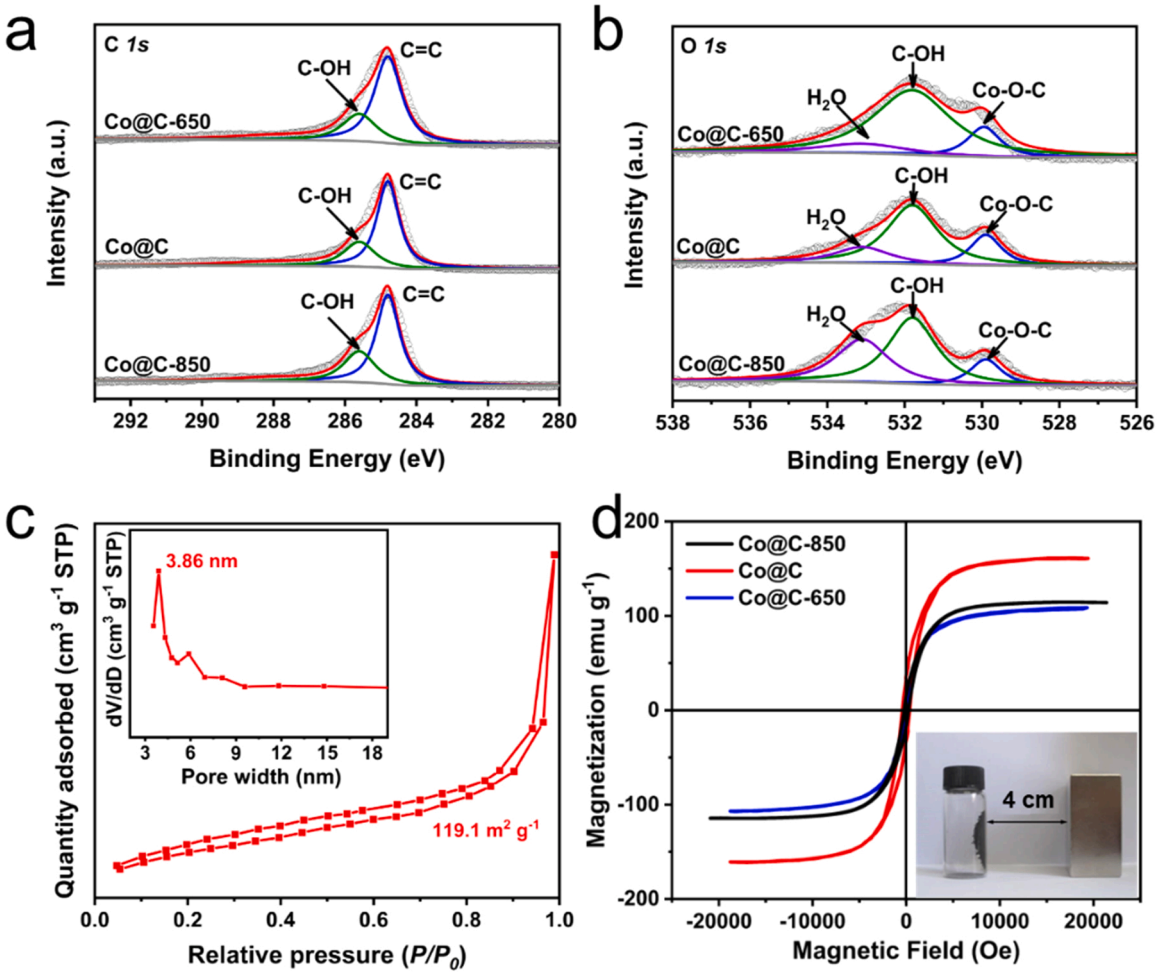

Fig. 2. High-resolution XPS spectra of (a) C *1s* and (b) O *1s* for Co@C and control samples. (c) N_2 adsorption/desorption isotherm and pore size distributions (inset) of Co@C. (d) Magnetic hysteresis loops of Co@C, Co@C-650 and Co@C-850. The inset of (d) is a photograph of Co@C nanorods under an external magnetic field.

H_2O nanorods at 750 °C under inert atmosphere, Co@C nanorods which maintained the original 1D nanorod morphology of the precursor were obtained (Fig. 1a). The graphitic carbon derived from the carbonization of interlayer salicylate in-situ encapsulates the cobalt species, remitting the further agglomeration [27]. Transmission electron microscopy (TEM) and high-resolution TEM (HRTEM) images further demonstrate that the Co NPs were about 20 nm in size, which homogeneously dispersed on the 1D nanorods and were completely embedded in the graphitic carbon matrix (Fig. 1b, c). The lattice distances of about 0.204 nm and 0.34 nm correspond to the (111) plane of face-centered cubic Co and graphitic carbon shell, respectively [28]. The crystalline structure of the obtained Co@C was examined by powder X-ray diffraction (XRD) (Fig. 1d). Three sharp peaks at about 44°, 51° and 76° are assigned to the (111), (200) and (220) planes of cobalt (JCPDS 15–0806), respectively. Additionally, the appearance of weak diffraction at about 26° was attributed to the graphite carbon. No other peaks of impurities such as carbide or oxide was detected, suggesting the purity of Co@C product. Raman spectrum (Fig. 1e) of Co@C with two prominent bonds of defective and graphitic carbons at D (1345 cm^{-1}) and G (1584 cm^{-1}) confirms the formation of highly defective graphitic structure based on the intensity ratios of I_D/I_G[29]. The energy dispersive X-ray (EDX) spectrum shows that Co@C only contains cobalt, oxygen, and carbon (Fig. 1f). More importantly, this strategy for the synthesis of Co@C can be easily scaled up. For instance, in a typical synthetic procedure, 5.0 g Co@C was obtained in a single batch (inset of Fig. 1f), indicating the great potential in practical applications. In addition, the size of Co NPs in the Co@C is tunable by only changing the pyrolysis temperature. The samples synthesized at 650 and 850 °C, denoted as Co@C-x, (x = 650 and 850) show similar morphology to Co@C synthesized at 750 °C, except that the size of carbon-encapsulated NPs was about 7 nm and 40 nm for Co@C-650 and Co@C-850, respectively (Fig. S3).

3.2. *Rational designed chemical environment and strong magnetism of Co@C*

To further investigate the oxidation state and chemical environment of the Co@C nanorods, X-ray photoelectron spectroscopy (XPS) measurements were performed. For all three samples, both the deconvoluted high-resolution C *1s* spectrum and O *1s* spectrum (Fig. 2a and b) showed the existence of the abundant hydrophilic C-OH groups, which made a hydrophilic surface of the catalysts and facilitate the mass transport and catalytic efficiency of the reactions in aqueous solutions [30–32]. Besides, the presence of C—O—Co bonds in O *1s* spectrum indicate strong connections of Co species and C matrix, which prevents the aggregation of the Co NPs and benefits the electron transport between Co NPs and graphitic carbon shell, ensuring a high activity and stability of the catalyst [33]. Moreover, in the Co *2p* XPS spectrum in Fig. S4, the peaks belong to the metallic Co mostly invisible (778.7 eV and 793.7 eV) in Co@C and Co@C-850, implying that the metallic Co was entirely encapsulated by graphite carbon shell at higher pyrolysis temperatures [34]. Besides, the presence of two peaks at 781.0 and 797.0 eV corresponds to Co(II) species, demonstrated that the strong interaction exists between cobalt nanoparticles and O-rich carbon skeleton (Co—O bond), which accordingly leads to a lower electron density at the metallic Co

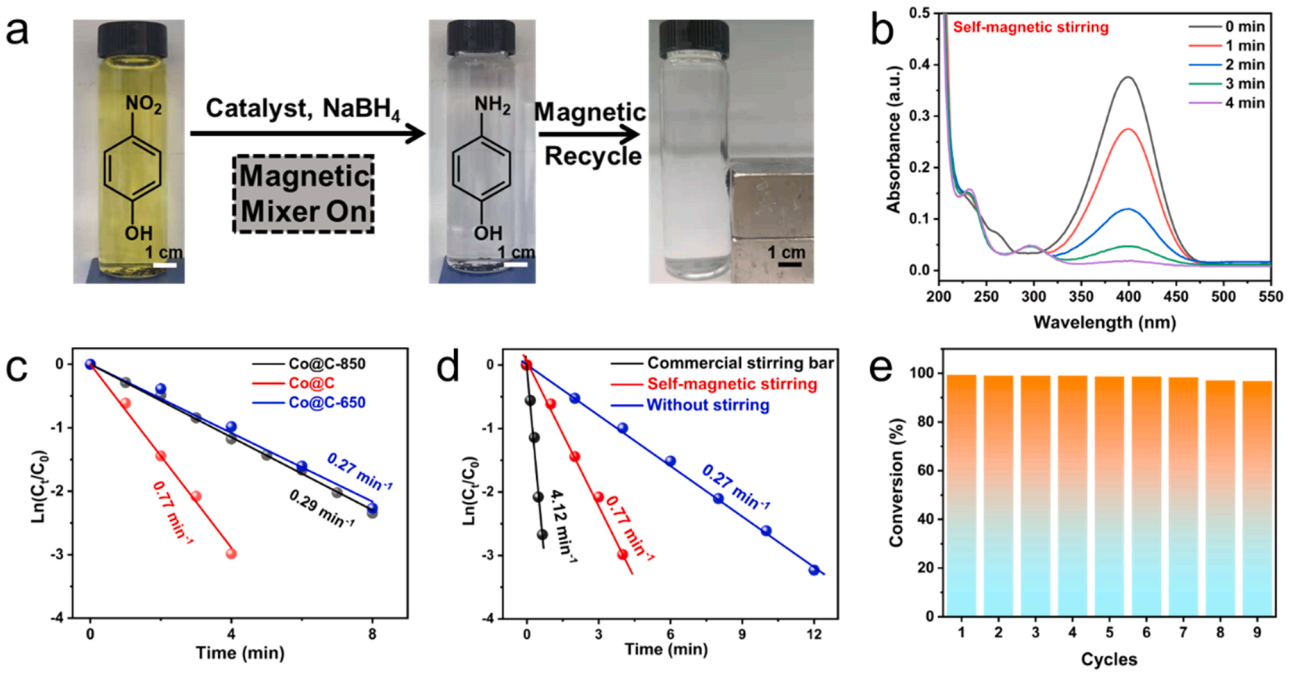

Fig. 3. (a) Magnetic stirring and recycling of Co@C during catalysis. (b) UV–vis spectra of the reduction reaction of 4-NP using Co@C as the catalyst and magnetic stirring nanobars. The relationship between $\ln(C_t/C_0)$ and reaction time of obtained samples (c) and different conditions (d). (e) Conversion of 4-NP in nine successive cycles of reduction after 4 min on Co@C.

sites [35,36]. Moreover, similar elemental composition and contents were found for three samples by XPS and inductively coupled plasma atomic emission spectroscopy (ICP-AES) (Table S1 and S2). Fourier-transform infrared (FT-IR) spectroscopy was applied to identify the functional groups of the as-obtained Co@C nanorods (Fig. S5). The peaks at 3423 cm^{-1}, 1457 cm^{-1}, and 1046 cm^{-1} can be assigned to O—H, C—O—(Co) and C—OH bands, respectively [37,38], which consistent well with the XPS results. Besides, the loss of cobalt species in Co@C after 3 h nitrohydrochloric acid treatment determined by ICP-AES is less than 0.02 wt%, indicating the favorable protection from the completely encapsulated carbon shell (Table S3). The Brunauer-Emmett-Teller (BET) specific surface area of the Co@C nanorods was determined to be 119.1 $m^2\ g^{-1}$ and the pore size distribution calculated by the Barrett-Joyner-Halenda (BJH) shows a peak centered at about 3.86 nm (Fig. 2c). With the increasing pyrolysis temperature, the specific surface area decreased slightly, however, the distribution of pore size showed no obvious difference between Co@C and control samples (Fig. S6). The large specific surface area increases the exposed active sites, and the mesoporous structures are beneficial to the mass transport of the reactant, which can further enhance the catalytic performance [39].

The magnetic properties of Co@C were measured by a vibrating sample magnetometer (VSM), which demonstrated an excellent magnetic property with a large saturation magnetization (M_s). As shown in the magnetic hysteresis loop in Fig. 2d, Co@C nanorods exhibit a M_s of 153.8 emu g^{-1}, which is approximately the same with bulk cobalt (163 emu g^{-1}) [40] and much larger than that of Co@C-650, Co@C-850 and state-of-art stirring catalysts (Table S4). A large magnetization indicates that a large magnetic force can be exerted under a low magnetic field, which is paramount for nanoscale stirring bars for energy saving. The obtained catalysts show superparamagnetic property owing to the completely encapsulated graphite carbon shell, which means they can be readily magnetized and manipulated by an applied magnetic field and lose magnetization immediately after removal of the magnetic field, thus avoiding agglomeration in a suspension in practical applications [41]. Based on the above, 1D Co@C nanorods with superior magnetic susceptibility and stability offer great potential for use as stirring nanobars. As shown in Movie S1 and Fig. S7, the Co@C aligned in the direction of the external magnetic field of a magnetic mixer, stirred with the magnetic field rotating after turning on the magnetic mixer, and stopped immediately as the magnetic mixer turned off.

Supplementary material related to this article can be found online at doi:10.1016/j.apcatb.2021.120925.

3.3. Superior catalytic activity as both magnetic stirring nanobars and nanocatalysts

Considering the unique structure and superior magnetic property, Co@C could serve as both high-performance catalysts and magnetic stirring nanobars for micro-catalytic reactions. We first evaluated the catalytic activity of Co@C by using the reduction of 4-nitrophenol (4-NP) to 4-aminophenol (4-AP) by $NaBH_4$ as a model reaction. As illustrated in Fig. 3a, the Co@C nanorods act as both high-performance catalysts and efficient magnetic stirring mixers under a rotating magnetic field. After the addition of as-prepared catalysts into the mixture of 4-NP and $NaBH_4$, the adsorption band of 4-NP at 400 nm significantly decreased as the reaction occurred within 1 min (Fig. 3b). While no obvious color changes can be found in the blank control system after 2 h (Fig. S8). The selectivity of the reduction product 4-AP from 4-NP is higher than 99% based on the liquid chromatography-mass spectrometry (LC-MS) analysis (Fig. S9). Fig. 3c shows the plot of ln (C_t) (C_t = concentration at time t) versus reaction time for the reduction reaction on as-obtained catalysts. The linear relations of ln (C_t/C_0) versus time were observed for all catalysts, indicating that the reactions followed first-order kinetics [42]. The rate constant k calculated from the rate equation ln (C_t/C_0) = kt was determined to be 0.77 min^{-1} for Co@C, which is much higher than the rate constants for Co@C-650 °C (0.27 min^{-1}) and Co@C-850 °C (0.29 min^{-1}) (Fig. S10), demonstrating the importance of the homogeneous distribution of completely carbon encapsulated metal nanoparticles. To demonstrate the magnetic stirring effect of Co@C as a nanoscale stirring bar, catalytic reaction with commercial stirring bar and without the stirring are also compared (Fig. 3d, Fig. S11). The rate constant k of Co@C was reduced by 2.85-folds, indicating an outstanding stirring ability of Co@C to boost

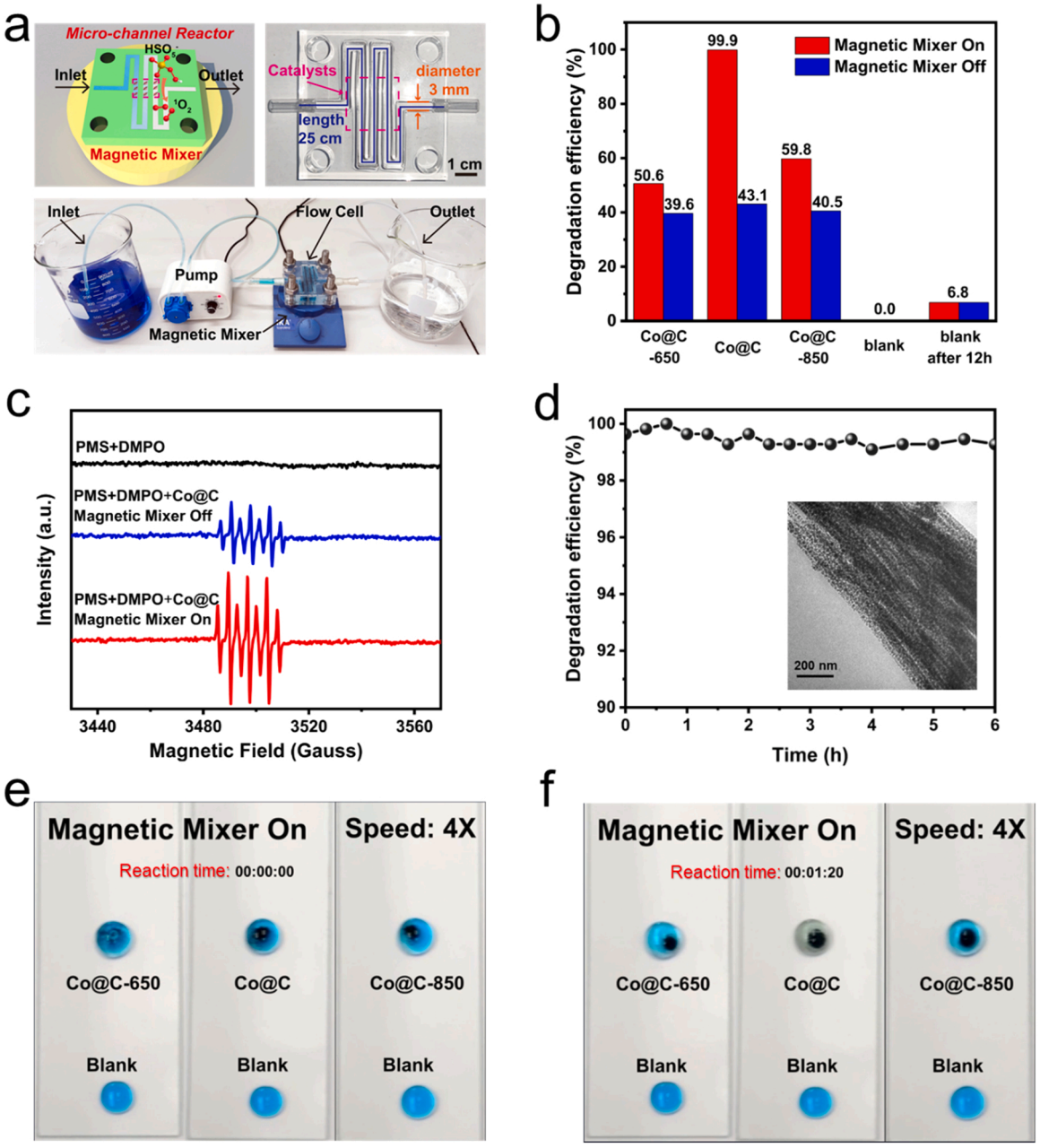

Fig. 4. (a) The schematic diagram and digital photograph of home-made Fenton-like flow cell. (b) The degradation efficiency of the catalysts. (c) EPR spectra of Co@C with magnetic mixer on/off and without catalysts. (d) The degradation efficiency of Co@C after 6 h continuous reaction (inset: TEM image of Co@C after catalysis). Snapshots in Movie S2 showing the degradation of dye solution (MB) in a water droplet (40 μL) before (e) and after (f) catalysis under the condition of magnetic mixer on.

the diffusion of the reactants. Moreover, the catalysts can be easily recycled by an external magnet after the catalytic reduction, which further eliminates the inevitable loss of the catalyst during the recycled process. After nine successive cycles of reaction, the conversion efficiency is around 100%, indicating the excellent stability of the catalyst (Fig. 3e).

3.4. Micro-system application: fast generation of singlet oxygen

Inspired by the micro-vortex derived from the nanorod, we envisioned that it can be used as stirring nanobars in a microsystem for rapid diffusion of the reactants. Sulfate radical (SO_4^-) based Fenton-like devices are considered as ideal household equipment for disinfection and degradation of recalcitrant pollutants in neutral water due to the strong oxidizing capability of SO_4^- [43]. The degradation of methylene blue (MB) by Fenton-like reaction in the flow cell and microdroplets with obvious color change progress from blue to colorless was chosen as a probe reaction. The schematic diagram and digital photograph of a homemade flow cell were shown in Fig. 4a. The mixed solution of potassium monopersulfate triple salt (PMS) and MB was continuous through the flow cell with a flow rate of 5 mL min^{-1}. The outlet solution was measured by UV–vis spectrometer to monitor the concentration of MB through its absorption peak at 664 nm (Figs. S12 and S13). The degradation efficiency is defined as DE% = (C_{in}-C_{out})/C_{in}* 100% (C_{in} and C_{out} equal to the concentration at inlet and outlet of the flow cell). As shown in Fig. 4b, Co@C with magnetic mixer on shows the maximum degradation efficiency (99.9%), which is much higher than Co@C with the magnetic mixer off (43.1%), indicating the fast mass transport

derived from magnetic stirring nanobars. The blank sample after 12 h was collected, the degradation efficiency of 6.8% indicates the importance of the catalysts. DMPO (5,5-dimethyl-1-pyrroline *N*-oxide) trapped electron paramagnetic resonance (EPR) experiments were further conducted to identify the active radical species in the Fenton-like reaction. Without the catalyst, no EPR signal was detected. After introducing Co@C into the reaction system with the magnetic mixer off, the new peaks assigned to DMPOX adducts (5, 5-dimethyl-2-pyrrolidone--*N*-oxyl, with $A_N = 7.2$ G and $A_H = 4.1$ G), resulting from the reaction between $^1O_2$ (singlet oxygen) and DMPO [44] could be observed. Besides, 2,2,6,6-tetramethyl-4-pi-peridinyloxyl (TEMP) was employed to capture $^1O_2$, three peaks of TEMP-$^1O_2$ [45] were clearly detected in the EPR spectrum (Fig. S14a). Moreover, the Co@C with magnetic mixer on showed an obvious higher EPR signal, indicating the enhanced mass transport derived from the catalysts stirring. 9,10-diphenylanthracene (DPA) is considered as a chemical trapping reagent, which can react with $^1O_2$ to yield the transannular endoperoxide ($DPAO_2$) with high reaction rate constant [46]. As shown in Fig. S14b, the decrease of the absorption band for DPA in methanol (350–400 nm) demonstrate the generation of $^1O_2$, which consist well with the EPR results. These results demonstrate that the generated $^1O_2$ was active radical species during the Fenton-like reaction. Moreover, Co@C shows excellent stability. In a 6 h continuous stability test, 5 mg Co@C can degrade 1.8 L mixture of MB (1.25×10^{-5} mol L^{-1}) and PMS (2.7×10^{-4} mol L^{-1}) solution with degradation efficiency higher than 99% (Fig. 4d). The morphology of Co@C after 6 h of reaction was investigated, and no noticeable changes could be observed relative to the fresh sample (Fig. 4 inset and Fig. S15). Besides, the excellent chemical stability of Co@C was further confirmed by high-resolution XPS spectra (Fig. S16). The faster reaction rate of MB degradation should be ascribed to the superior catalytic activity and the mixing ability of Co@C. Moreover, the excellent performance of Co@C was demonstrated further in a microdroplet (Fig. 4e–f and Fig. S17). As shown in Movie S2, the blue microdroplets became colorless in 80 s after the addition of Co@C. In comparison, the fading rate of MB became obviously slower without the rotating external magnetic field (Movie S3). As a control sample, homogeneous Co ions shows negligible catalytic activity on methylene blue degradation after 20 min with the magnetic mixer on, indicating the high performance of Co@C (Fig. S18). In addition, tertbutanol (TBA) or methanol (radical scavenger for ·OH and $SO_4^{\cdot-}$, respectively) was added into the reaction mixture, the fading rate of MB decreased slightly (Fig. S19), which indicates the influence of ·OH and SO_4^{-} can be neglected[44] and verifies the generation of active radical species of $^1O_2$.

Supplementary material related to this article can be found online at doi:10.1016/j.apcatb.2021.120925.

4. Conclusions

In summary, we have successfully developed a novel, efficient and scalable strategy for fabricating 1D Co@C nanorods as both high-performance catalysts and nanoscale magnetic stirring bars. The obtained magnetic nanorods exhibit uniform diameter (–100 nm), large mesopores (–3.4 nm), and high surface area (119.1 m^2 g^{-1}). The Co NPs were encapsulated by graphitic carbon shell, which avoids the loss of active species during the catalytic process. Co@C nanorods with superior saturation magnetization (153.8 emu g^{-1}) exhibit high susceptibility to an applied magnetic field with an easy alignment and rotation, which can be directly used as nanoscale magnetic stirring bars.

CRediT authorship contribution statement

Tianyu Zhang: Conceptualization, Methodology, Investigation, Data curation, Writing – original draft. **Huijing Wang**: Conceptualization, Methodology, Investigation, Data curation, Writing – original draft. **Xiaodi Guo**: Formal analysis. **Shiheng Shao**: Formal analysis. **Lei Ding**: Investigation. **Aijuan Han**: Writing – review & editing. **Lianying Wang**: Writing – review & editing. **Junfeng Liu**: Conceptualization, Project administration, Supervision, Writing – review & editing.

Declaration of Competing Interest

The authors declare that they have no known competing financial interests or personal relationships that could have appeared to influence the work reported in this paper.

Acknowledgements

This study was supported by the National Natural Science Foundation of China, China (NSFC) and Fundamental Research Funds for the Central Universities, China.

Appendix A. Supporting information

Supplementary data associated with this article can be found in the online version at doi:10.1016/j.apcatb.2021.120925.

References

[1] D. Schneider, D. Mehlhorn, P. Zeigermann, J. Kärger, R. Valiullin, Transport properties of hierarchical micro-mesoporous materials, Chem. Soc. Rev. 45 (2016) 3439–3467.
[2] L. Mao, H. Koser, Towards ferrofluidics for μ-TAS and lab on-a-chip applications, Nanotechnology 17 (2006) S34–S47.
[3] A.J. deMello, Control and detection of chemical reactions in microfluidic systems, Nature 442 (2006) 394–402.
[4] E.O. Pentsak, D.B. Eremin, E.G. Gordeev, V.P. Ananikov, Phantom reactivity in organic and catalytic reactions as a consequence of microscale destruction and contamination-trapping effects of magnetic stir bars, ACS Catal. 9 (2019) 3070–3081.
[5] Z. Gu, X. An, R. Liu, L. Xiong, J. Tang, C. Hu, H. Liu, J. Qu, Interface-modulated nanojunction and microfluidic platform for photoelectrocatalytic chemicals upgrading, Appl. Catal. B Environ. 282 (2021), 119541.
[6] Z. Gu, X. An, H. Lan, Y. Tian, J. Zhang, R. Liu, H. Liu, J. Qu, Microfluidic-enhanced 3-D photoanodes with free interfacial energy barrier for photoelectrochemical applications, Appl. Catal. B Environ. 244 (2019) 740–747.
[7] W.H. Chong, L.K. Chin, R.L.S. Tan, H. Wang, A.Q. Liu, H. Chen, Stirring in suspension: nanometer-sized magnetic stir bars, Angew. Chem. Int. Ed. 52 (2013) 8570–8573.
[8] S. Yang, C. Cao, Y. Sun, P. Huang, F. Wei, W. Song, Nanoscale magnetic stirring bars for heterogeneous catalysis in microscopic systems, Angew. Chem. Int. Ed. 54 (2015) 2661–2664.
[9] J. Yuan, Y. Xu, A.H.E. Müller, One-dimensional magnetic inorganic–organic hybrid nanomaterials, Chem. Soc. Rev. 40 (2011) 640–655.
[10] L. He, M. Wang, J. Ge, Y. Yin, Magnetic assembly route to colloidal responsive photonic nanostructures, Acc. Chem. Res. 45 (2012) 1431–1440.
[11] I. Jung, S. Ih, H. Yoo, S. Hong, S. Park, Fourier transform surface plasmon resonance of nanodisks embedded in magnetic nanorods, Nano Lett. 18 (2018) 1984–1992.
[12] S. Shylesh, V. Schünemann, W.R. Thiel, Magnetically separable nanocatalysts: bridges between homogeneous and heterogeneous catalysis, Angew. Chem. Int. Ed. 49 (2010) 3428–3459.
[13] X. Zhou, C. Chen, C. Cao, T. Song, H. Yang, W. Song, Enhancing reaction rate in a Pickering emulsion system with natural magnetotactic bacteria as nanoscale magnetic stirring bars, Chem. Sci. 9 (2018) 2575–2580.
[14] Q. Ji, T. Hu, Q. Chen, W. Xin, X. Liu, H. Chen, Scalable and continuous preparation of nano-stirbars by electrospinning, Chem. Commun. 56 (2020) 11767–11770.
[15] S. Yang, C. Cao, L. Peng, P. Huang, Y. Sun, F. Wei, W. Song, Spindle-shaped nanoscale yolk/shell magnetic stirring bars for heterogeneous catalysis in macro- and microscopic systems, Chem. Commun. 52 (2016) 1575–1578.
[16] S. Wang, J. Fu, K. Wang, M. Gao, X. Wang, Z. Wang, J. Chen, Q. Xu, Facile synthesis of Pd nanoparticles on polydopamine-coated Fe-Fe_2O_3 magnetic nanochains as recyclable high-performance nanocatalysts, Appl. Surf. Sci. 459 (2018) 208–216.
[17] L. Xu, H.-W. Liang, Y. Yang, S.-H. Yu, Stability and reactivity: positive and negative aspects for nanoparticle processing, Chem. Rev. 118 (2018) 3209–3250.
[18] E.T. Yun, S.W. Park, H.J. Shin, H. Lee, D.W. Kim, J. Lee, Peroxymonosulfate activation by carbon-encapsulated metal nanoparticles: switching the primary reaction route and increasing chemical stability, Appl. Catal. B Environ. 279 (2020), 119360.
[19] X. Ren, S. Wei, Q. Wang, L. Shi, X.S. Wang, Y. Wei, G. Yang, D. Philo, F. Ichihara, J. Ye, Rational construction of dual cobalt active species encapsulated by ultrathin carbon matrix from MOF for boosting photocatalytic H_2 generation, Appl. Catal. B Environ. 286 (2021), 119924.
[20] M.B. Gawande, A. Goswami, T. Asefa, H. Guo, A.V. Biradar, D.-L. Peng, R. Zboril, R.S. Varma, Core–shell nanoparticles: synthesis and applications in catalysis and electrocatalysis, Chem. Soc. Rev. 44 (2015) 7540–7590.

[21] S.H. Moon, S.-h Noh, J.-H. Lee, T.-H. Shin, Y. Lim, J. Cheon, Ultrathin interface regime of core–shell magnetic nanoparticles for effective magnetism tailoring, Nano Lett. 17 (2017) 800–804.
[22] Q. Wei, F. Xiong, S. Tan, L. Huang, E.H. Lan, B. Dunn, L. Mai, Porous one-dimensional nanomaterials: design, fabrication and applications in electrochemical energy storage, Adv. Mater. 29 (2017) 1602300.
[23] K.-C. Ho, L.-Y. Lin, A review of electrode materials based on core–shell nanostructures for electrochemical supercapacitors, J. Mater. Chem. A 7 (2019) 3516–3530.
[24] T. Jin, Q. Han, Y. Wang, L. Jiao, 1D nanomaterials: design, synthesis, and applications in sodium–ion batteries, Small 14 (2018) 1703086.
[25] X. Yan, M. Gu, Y. Wang, L. Xu, Y. Tang, R. Wu, In-situ growth of Ni nanoparticle-encapsulated N-doped carbon nanotubes on carbon nanorods for efficient hydrogen evolution electrocatalysis, Nano Res. 13 (2020) 975–982.
[26] X. Guo, L. Wang, S. Yue, D. Wang, Y. Lu, Y. Song, J. He, Single-crystalline organic–inorganic layered cobalt hydroxide nanofibers: facile synthesis, characterization, and reversible water-induced structural conversion, Inorg. Chem. 53 (2014) 12841–12847.
[27] T. Zhang, X. Han, H. Yang, A. Han, E. Hu, Y. Li, X.-q Yang, L. Wang, J. Liu, B. Liu, Atomically dispersed nickel(I) on an alloy-encapsulated nitrogen-doped carbon nanotube array for high-performance electrochemical CO_2 reduction reaction, Angew. Chem. Int. Ed. 59 (2020) 12055–12061.
[28] Z. Lu, W. Xu, J. Ma, Y. Li, X. Sun, L. Jiang, Superaerophilic carbon-nanotube-array electrode for high-performance oxygen reduction reaction, Adv. Mater. 28 (2016) 7155–7161.
[29] S. Chen, Y. Feng, J. Wang, E. Zhang, X. Yu, B. Lu, Free-standing N-doped hollow carbon fibers as high-performance anode for potassium ion batteries, Sci. China Mater. 64 (2021) 547–556.
[30] L. Zhang, Y. Ding, C. Zhang, Y. Zhou, X. Zhou, Z. Liu, G. Yu, Enabling graphene-oxide-based membranes for large-scale energy storage by controlling hydrophilic microstructures, Chem 4 (2018) 1035–1046.
[31] D. Xiang, X. Bo, X. Gao, C. Zhang, C. Du, F. Zheng, Z. Zhuang, P. Li, L. Zhu, W. Chen, Novel one-step synthesis of core@shell iron–nickel alloy nanoparticles coated by carbon layers for efficient oxygen evolution reaction electrocatalysis, J. Power Sources 438 (2019), 226988.
[32] X.-k Kong, Q.-w Chen, Z.-y Lun, Probing the influence of different oxygenated groups on graphene oxide's catalytic performance, J. Mater. Chem. A 2 (2014) 610–613.
[33] M. Leng, X. Huang, W. Xiao, J. Ding, B. Liu, Y. Du, J. Xue, Enhanced oxygen evolution reaction by Co—O—C bonds in rationally designed Co_3O_4/graphene nanocomposites, Nano Energy 33 (2017) 445–452.
[34] Y. Tu, H. Li, D. Deng, J. Xiao, X. Cui, D. Ding, M. Chen, X. Bao, Low charge overpotential of lithium-oxygen batteries with metallic Co encapsulated in single-layer graphene shell as the catalyst, Nano Energy 30 (2016) 877–884.
[35] Y. Liang, Y. Li, H. Wang, J. Zhou, J. Wang, T. Regier, H. Dai, Co_3O_4 nanocrystals on graphene as a synergistic catalyst for oxygen reduction reaction, Nat. Mater. 10 (2011) 780–786.
[36] Z. Wei, J. Wang, S. Mao, D. Su, H. Jin, Y. Wang, F. Xu, H. Li, Y. Wang, In situ-generated Co_0-Co_3O_4/N-doped carbon nanotubes hybrids as efficient and chemoselective catalysts for hydrogenation of nitroarenes, ACS Catal. 5 (2015) 4783–4789.
[37] X. Sun, Y. Li, Colloidal carbon spheres and their core/shell structures with noble-metal nanoparticles, Angew. Chem. Int. Ed. 43 (2004) 597–601.
[38] T.-F. Yeh, J.-M. Syu, C. Cheng, T.-H. Chang, H. Teng, Graphite oxide as a photocatalyst for hydrogen production from water, Adv. Funct. Mater. 20 (2010) 2255–2262.
[39] M. Khayet, A. Velázquez, J.I. Mengual, Modelling mass transport through a porous partition: effect of pore size distribution, J. Non-Equilib. Thermodyn. 29 (2004) 279–299.
[40] A.-H. Lu, W.-C. Li, A. Kiefer, W. Schmidt, E. Bill, G. Fink, F. Schüth, Fabrication of magnetically separable mesostructured silica with an open pore system, J. Am. Chem. Soc. 126 (2004) 8616–8617.
[41] L. Wan, H. Song, X. Chen, Y. Zhang, Q. Yue, P. Pan, J. Su, A.A. Elzatahry, Y. Deng, A magnetic-field guided interface coassembly approach to magnetic mesoporous silica nanochains for osteoclast-targeted inhibition and heterogeneous nanocatalysis, Adv. Mater. 30 (2018) 1707515.
[42] Z. Ji, X. Shen, G. Zhu, H. Zhou, A. Yuan, Reduced graphene oxide/nickel nanocomposites: facile synthesis, magnetic and catalytic properties, J. Mater. Chem. 22 (2012) 3471–3477.
[43] W.-D. Oh, Z. Dong, T.-T. Lim, Generation of sulfate radical through heterogeneous catalysis for organic contaminants removal: current development, challenges and prospects, Appl. Catal. B Environ. 194 (2016) 169–201.
[44] X. Li, X. Huang, S. Xi, S. Miao, J. Ding, W. Cai, S. Liu, X. Yang, H. Yang, J. Gao, Single cobalt atoms anchored on porous N-doped graphene with dual reaction sites for efficient Fenton-like catalysis, J. Am. Chem. Soc. 140 (2018) 12469–12475.
[45] L. Zhang, X. Jiang, Z. Zhong, L. Tian, Q. Sun, Y. Cui, X. Lu, J. Zou, S. Luo, Carbon nitride supported high-loading Fe single-atom catalyst for activating of peroxymonosulfate to generate $^1O_2$ with 100% selectivity, Angew. Chem. Int. Ed. 60 (2021) 21751–21755.
[46] M. Burguete, F. Galindo, R. Gavara, S. Luis, M. Moreno, P. Thomas, D. Russel, Singlet oxygen generation using a porous monolithic polymer supported photosensitizer: potential application to the photodynamic destruction of melanoma cells, Photochem. Photobiol. Sci. 8 (2009) 37–44.